

# Equilibrium $\beta$ -limits dependence on bootstrap current in classical stellarators

A. Baillod <sup>ID 1</sup>,<sup>†</sup> J. Loizu <sup>ID 1</sup>, Z.S. Qu <sup>ID 2</sup>, H.P. Arbez <sup>1</sup> and J.P. Graves <sup>ID 1</sup>

<sup>1</sup>Ecole Polytechnique Fédérale de Lausanne, Swiss Plasma Center, CH-1015 Lausanne, Switzerland

<sup>2</sup>School of Physical and Mathematical Sciences, Nanyang Technological University, 637371 Singapore, Republic of Singapore

(Received 12 December 2022; revised 11 August 2023; accepted 14 August 2023)

While it is important to design stellarators with high magnetohydrodynamic stability  $\beta$ -limit, it is also crucial to ensure that good magnetic surfaces exist in a large range of  $\beta$  values. As  $\beta$  increases, pressure-driven currents perturb the vacuum magnetic field and often lead to the emergence of magnetic field line chaos, which can worsen the confinement and is the cause of another kind of  $\beta$ -limit, the so-called equilibrium  $\beta$ -limit. In this paper, we explore numerically the dependence of the equilibrium  $\beta$ -limit on the bootstrap current strength in a classical stellarator geometry using the stepped pressure equilibrium code. We develop a diagnostic to determine whether or not magnetic islands are expected to participate significantly to radial transport, and we build an analytical model to predict the expected equilibrium  $\beta$ -limit, which recovers the main features of the numerical results. This research opens the possibility to include additional targets in stellarator optimization functions, provides additional understanding on the existence of magnetic surfaces at large  $\beta$ , and is a step forward in the understanding of the equilibrium  $\beta$ -limit.

**Key words:** plasma confinement, plasma nonlinear phenomena, plasma simulation

---

## 1. Introduction

In magnetic fusion devices such as stellarators, zeroth-order confinement of particles and energy is obtained by constructing an equilibrium with magnetic surfaces. Magnetic islands and magnetic field line chaos can be detrimental to confinement, i.e. they can contribute to the radial transport of particle and energy (Hudson & Nakajima 2010). While it is possible to design equilibria with good magnetic surfaces in a vacuum (Cary & Kotschenreuther 1985; Cary & Hanson 1986; Pedersen *et al.* 2016), pressure-driven plasma currents, such as diamagnetic, Pfirsch–Schlüter and bootstrap currents, perturb finite pressure equilibria, and, at a sufficiently large pressure, magnetic islands and chaos emerge.

<sup>†</sup> Email address for correspondence: [antoine.baillod@epfl.ch](mailto:antoine.baillod@epfl.ch)

A pressure increase can also sometimes heal magnetic islands (Bhattacharjee *et al.* 1995). While this mechanism can improve confinement locally, other islands might open elsewhere in the plasma as  $\beta$  increases. There is thus a critical value of  $\beta$  at which magnetic islands open and magnetic field line chaos emerges. This defines an equilibrium  $\beta$ -limit. Note, however, that the equilibrium  $\beta$ -limit is a ‘soft’ limit, since crossing it does not lead to a loss of control of the plasma. Additional input power may, however, leak through the damaged magnetic surfaces more easily (Rechester & Rosenbluth 1978), thereby preventing an increase of  $\beta$ . Crossing the equilibrium  $\beta$ -limit may thus not be as concerning as crossing a stability limit (which may lead to plasma disruptions), but it still limits the overall performance of the reactor. It is consequently of crucial importance to understand these equilibrium  $\beta$ -limits better, especially for the operation of existing experiments and the design of new machines. Configurations where good magnetic surfaces are preserved over a large range of  $\beta$  have to be sought, which will help to ultimately identify configurations with large enough equilibrium  $\beta$ -limit.

In the case of a classical stellarator, Loizu *et al.* (2017) proposed a model for the equilibrium  $\beta$ -limit of a configuration with zero net toroidal current as well as one with a fixed edge rotational transform. Other studies computed high  $\beta$  equilibria in a number of experimentally relevant stellarator configurations and predicted the emergence of magnetic field line chaos at sufficiently large  $\beta$  – see, for example, the calculation by Suzuki, Watanabe & Sakakibara (2020) in the Large Helical Device and Reiman *et al.* (2007) in Wendelstein 7-AS (W7-AS). However, to the authors’ knowledge, no attempt has been made to analytically model the impact of the bootstrap current on the equilibrium  $\beta$ -limit, and to determine how this critical  $\beta$  depends on the device parameters.

We propose to extend the work of Loizu *et al.* (2017) to the case of a classical stellarator with bootstrap current. We use the stepped pressure equilibrium code (SPEC) to compute a large number of free-boundary equilibria at different  $\beta$ , including the effect of bootstrap current. The code SPEC has been chosen for its speed, its capability to describe equilibria with magnetic islands and chaos, and the possibility to calculate free-boundary equilibria (Hudson *et al.* 2020) with a constrained toroidal current profile (Baillod *et al.* 2021). The code SPEC has been verified in stellarator geometry (Loizu, Hudson & Nührenberg 2016b), and its core algorithm has been improved to run faster and to be more robust (Qu *et al.* 2020b). It has been successfully applied to study current sheets at rational surfaces (Loizu *et al.* 2015a,b; Huang *et al.* 2022), ideal linear instabilities (Kumar *et al.* 2021, 2022), tearing mode stability (Loizu & Hudson 2019) and nonlinear saturation (Loizu *et al.* 2020), penetration of resonant magnetic perturbations in the ideal limit (Loizu *et al.* 2016a) and relaxation phenomena in reversed field pinches (Dennis *et al.* 2013b, 2014; Qu *et al.* 2020a).

To numerically identify the equilibrium  $\beta$ -limit, Loizu *et al.* used a diagnostic based on the volume of chaos, i.e. the volume of plasma occupied by chaotic field lines, which were identified by measuring their fractal dimension (Meiss 1992). However, this approach is too pessimistic since some chaotic magnetic field lines might be able to preserve confinement (Hudson & Breslau 2008). An alternative approach, proposed by Paul, Hudson & Helander (2022), is to measure the effective volume of parallel diffusion. This measures the fraction of plasma volume over which the local parallel transport dominates over the perpendicular one in setting the radial transport. Contrary to the volume of chaos, this approach takes into account only sufficiently large resonances that do participate significantly to the radial transport. In this paper, we follow Paul *et al.* and measure the equilibrium  $\beta$ -limit by taking the  $\beta$  above which the radial transport generated by damaged magnetic surfaces represents a significant fraction of the total radial transport.

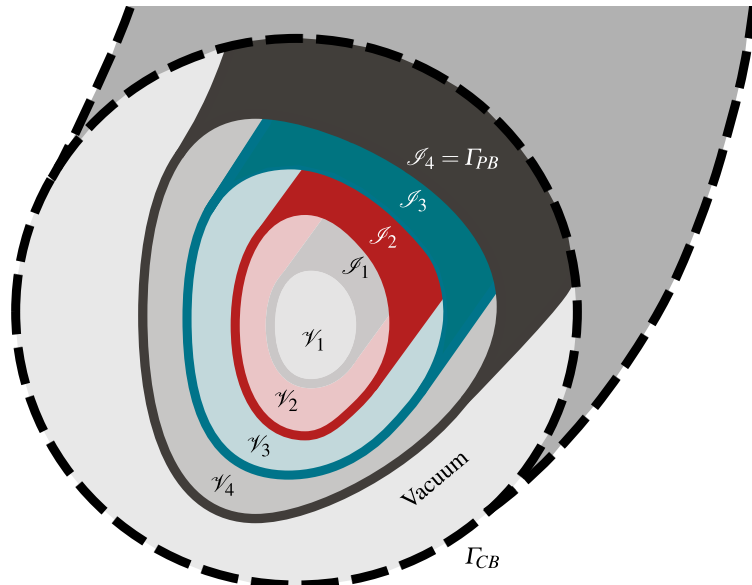


FIGURE 1. Sketch of a SPEC equilibrium with four volumes. The plasma boundary,  $\Gamma_{PB} = \mathcal{I}_4$ , is the dark grey surface and the computational boundary;  $\Gamma_{CB}$ , is the light grey surface.

This paper is organized as follows. In § 2, the equations solved by SPEC are recalled. In § 3, we construct free-boundary equilibria in a rotating ellipse geometry, and construct a bootstrap current model. In § 4, a new diagnostic is developed to measure the equilibrium  $\beta$ -limit and compared with the volume of chaos. In § 5, we derive an analytical model to explain the numerically obtained equilibrium  $\beta$ -limit. Finally, some concluding remarks are provided in § 6.

## 2. The stepped-pressure equilibrium code

The code SPEC finds three-dimensional free-boundary magnetohydrodynamic (MHD) equilibria with stepped-pressure profiles. Pressure steps are supported by a finite number of nested toroidal surfaces  $\mathcal{I}_l$ , thereby defining  $N_{\text{vol}}$  nested volumes  $\mathcal{V}_l$  with constant pressure  $p_l$ , with  $l \in \{1, \dots, N_{\text{vol}}\}$  (see figure 1).

The magnetic field  $\mathbf{B}$  in each volume is allowed to reconnect and can form magnetic islands and chaotic field lines, while the volume interfaces are constrained to be nested magnetic surfaces. The magnetic field in each volume is a force-free field described by a Taylor state (Taylor 1974, 1986),

$$\nabla \times \mathbf{B} = \mu_l \mathbf{B}, \quad (2.1)$$

with  $\mu_l$  a constant specific to the volume  $\mathcal{V}_l$ , and the solution to (2.1) depends on the geometry of the interfaces enclosing the volume  $\mathcal{V}_l$ . The code SPEC finds the geometries of interfaces  $\mathcal{I}_l$  such that force balance is satisfied,

$$\left[ \left[ p + \frac{B^2}{2\mu_0} \right] \right]_l = 0, \quad (2.2)$$

where  $\mu_0$  is the vacuum permeability,  $p$  is the pressure and  $[[\cdot]]_l$  denotes the jump across the interface  $\mathcal{I}_l$ . Equation (2.2) is the local equivalent to the more common force-balance condition  $\mathbf{j} \times \mathbf{B} = \nabla p$ .

The last interface defines the plasma boundary  $\Gamma_{\text{PB}}$ . The plasma is surrounded by a vacuum region (where  $p_l = 0$  and  $\mu_l = 0$ ), itself bounded by a computational boundary  $\Gamma_{\text{CB}}$  that lies outside the plasma and inside the coils. The toroidal surface  $\Gamma_{\text{CB}}$  is an otherwise arbitrary mathematical surface and not necessarily a magnetic surface, i.e. generally  $\mathbf{B} \cdot \mathbf{n} \neq 0$  on  $\Gamma_{\text{CB}}$ , with  $\mathbf{n}$  a vector normal to  $\Gamma_{\text{CB}}$ . Note that the plasma averaged  $\beta$  is evaluated from a SPEC equilibrium as

$$\beta = \frac{1}{V} \sum_{l=1}^{N_{\text{vol}}} 2\mu_0 p_l \iiint_V \frac{dv}{B^2}, \quad (2.3)$$

with  $V$  the volume enclosed by  $\Gamma_{\text{PB}}$ .

Free-boundary equilibria are determined by providing the total current flowing through the torus hole,  $I_c$ , the geometry of the computational boundary, and the harmonics of the vacuum field (produced by the coils) normal to the computational boundary. In addition, SPEC requires as input, in each volume, the enclosed toroidal flux  $\psi_{t,l}$ , the pressure  $p_l$ , the net toroidal current within the volume  $I_{\phi,l}^v$  (closely related to the constant  $\mu_l$ ), and the net toroidal current flowing at each interface  $I_{\phi,l}^s$ , which is a surface current.

Volume currents  $I_{\phi,l}^v$  represent all externally driven currents, such as ohmic current, electron cyclotron current drive or neutral beam current drive. Surface currents  $I_{\phi,l}^s$  are all pressure-driven currents, such as diamagnetic, Pfirsch–Schlüter or bootstrap current, or island shielding currents. Further details about the SPEC algorithm and implementation can be found in Hudson *et al.* (2012, 2020) and Baillod *et al.* (2021).

### 3. Rotating ellipse with bootstrap current

We study the case of a rotating ellipse (sometimes also called a classical stellarator) with an analytical bootstrap current model. While a rotating ellipse is arguably a simple geometry, it is still relevant since all stellarators without magnetic axis torsion are rotating ellipses close to the magnetic axis (Helander 2014). An experimental instance of rotating ellipse was, for example, the Wendelstein VII-A stellarator (Grieger, Renner & Wobig 1985).

We choose a computational boundary  $\Gamma_{\text{CB}}$  (see figure 2) using standard cylindrical coordinates  $\mathbf{x} = R_{\text{CB}}(\theta, \phi)\hat{\mathbf{e}}_R + Z_{\text{CB}}(\theta, \phi)\hat{\mathbf{e}}_Z$ , with

$$R_{\text{CB}}(\theta, \phi) = R_0 + R_{10} \cos(\theta) + R_{11} \cos(\theta - N_{\text{fp}}\phi), \quad (3.1)$$

$$Z_{\text{CB}}(\theta, \phi) = Z_{10} \sin(\theta) + Z_{11} \sin(\theta - N_{\text{fp}}\phi), \quad (3.2)$$

with  $N_{\text{fp}} = 5$  the number of field periods,  $R_0 = 10$  m,  $R_{10} = -Z_{10} = 1$  m,  $R_{11} = Z_{11} = 0.25$  m. The effective minor radius is  $a_{\text{eff}} = \sqrt{r_{\min} r_{\max}}$  with  $r_{\min} = R_{10} - R_{11}$  and  $r_{\max} = R_{10} + R_{11}$  the minor and major radii of the ellipse, respectively. We define  $\epsilon_a = a_{\text{eff}}/R_0$  as the inverse aspect ratio at the plasma boundary.

We assume that a coil system exists such that  $\mathbf{B}_c \cdot \mathbf{n} = B_v \hat{\mathbf{e}}_z \cdot \mathbf{n}$  on  $\Gamma_{\text{CB}}$ , where  $\mathbf{B}_c$  is the magnetic field produced by the coils, and  $B_v \hat{\mathbf{e}}_z$  is a constant vertical field, which is applied to keep the plasma within the computational boundary at high  $\beta$ . We set  $B_v = -0.03$  T. This vertical field has little to no impact on the results presented hereafter; its only purpose is to keep the plasma within the volume defined by  $\Gamma_{\text{CB}}$ . We fix the total current flowing in the torus hole to  $I_c = 17.1$  MA, which determines the toroidal flux enclosed by the computational boundary,  $\psi_{t,V} = 1$  Tm<sup>2</sup>.

We choose a pressure profile with a linear dependence on the toroidal flux, i.e.  $p = p_0(1 - \psi_t/\psi_a)$ , with  $p_0$  a free parameter and  $\psi_a = 0.25$  Tm<sup>2</sup> the total toroidal flux enclosed by the plasma boundary  $\Gamma_{\text{PB}}$ . We approximate the pressure profile with seven steps of equal

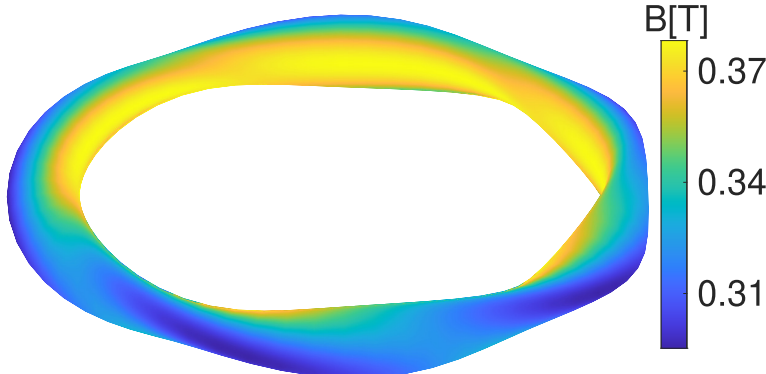


FIGURE 2. Computational boundary described by (3.1)–(3.2). Colours indicate the magnetic field strength in a vacuum.

magnitude  $[[p]]_l = p_0/N_{\text{vol}}$ . We thus define seven plasma regions, i.e.  $N_{\text{vol}} = 7$ , surrounded by a vacuum region. This means that  $\psi_{t,l} = (l - 1)\psi_a/N_{\text{vol}}$  and  $p_l = p(\psi_{t,l})$ . The number of volumes determines how the pressure profile is represented – more volumes means more and smaller pressure steps. As each interface is a discrete constraint on the magnetic topology, increasing the number of volumes reduces the available space for reconnection and thus the maximum size of magnetic islands and regions of magnetic field line chaos. In this paper, we are, however, interested in the onset of loss of magnetic surfaces, which is not affected by the volume available for islands to grow. Therefore, our results only depend weakly on the number of volumes (see the Appendix).

Two current profiles have to be provided to SPEC: the profile of volume currents,  $\{I_{\phi,l}^v\}$ , and the profile of surface currents  $\{I_{\phi,l}^s\}$  (see § 2). Here we study the case of an equilibrium with zero externally driven currents and with bootstrap current. No externally driven currents implies, in SPEC, that there are no currents in the plasma volumes, i.e.

$$I_{\phi,l}^v = 0. \quad (3.3)$$

The bootstrap current is a pressure-driven current, and is consequently described by a surface current at the volume's interfaces. We model it with

$$I_{\phi,l}^s = -C \left( \frac{\psi_{t,l}}{\psi_a} \right)^{1/4} [[p]]_l, \quad (3.4)$$

where  $(\psi_t/\psi_a)^{1/4} \approx \sqrt{\epsilon/\epsilon_a}$  is related to the fraction of trapped particles, with  $\epsilon$  the inverse aspect ratio;  $[[p]]_l$  is a measure of the local pressure gradient; and  $C$  is a coupling constant, in  $[\text{APa}^{-1}]$ , which controls the strength of the bootstrap current in the system. A full neoclassical calculation of the bootstrap current, for example with the SFINCS code (Landreman *et al.* 2014), would require the density and temperature profiles as inputs – and the freedom in the choice of the coupling constant  $C$  reflects the freedom in these profiles.

The current density associated with the current in (3.4) is

$$j_{\phi,l} = -\frac{C\psi_a}{\pi a_{\text{eff}}^2} \left( \frac{\psi_{t,l}}{\psi_a} \right)^{1/4} \frac{dp}{d\psi_t}. \quad (3.5)$$

Note that if

$$C = C_0 \equiv \frac{\sqrt{\epsilon_a} R_0}{\iota_v B_0}, \quad (3.6)$$

with  $\iota_v$  the edge rotational transform in vacuum and  $B_0$  such that  $\mu_0 I_c = 2\pi R_0 B_0$ , (3.5) reduces to the well-known large-aspect ratio tokamak bootstrap current approximation (Helander & Sigmar 2002),

$$j_\phi = \sqrt{\epsilon_a} R_0 \frac{dp}{d\psi_p}, \quad (3.7)$$

where  $\psi_p$  is the poloidal flux, and we made the approximation  $d\psi_p/d\psi_t = \iota \approx \iota_v$ . We normalize  $C$  by  $C_0$ , and define  $\hat{C} \equiv C/C_0$ . In the case of a large aspect ratio circular tokamak, we thus have  $\hat{C} = 1$ , while in a stellarator with no bootstrap current,  $\hat{C} = 0$ .

We use the recently implemented capability of SPEC to prescribe the toroidal current profile (Baillod *et al.* 2021), with the profiles defined in (3.3) and (3.4). Unless stated otherwise, the Fourier resolution used in all results presented in this paper is  $|n| \leq N = 12$ ,  $m \leq M = 12$ , with  $n$  the toroidal mode number and  $m$  the poloidal mode number, meaning that  $2[N + M(2N + 1)] + 1 = 625$  Fourier modes are used to describe each interface geometry. Results presented in this paper have been checked for convergence with respect to Fourier resolution (see the Appendix).

In summary, we can construct free-boundary SPEC equilibria with a simple bootstrap current model and we are left with two free parameters, namely (i)  $\beta$  which controls the total pressure in the system and (ii)  $\hat{C}$ , a dimensionless parameter, that controls the bootstrap current strength for a given plasma  $\beta$ .

### 3.1. Scans over $\hat{C}$ and $\beta$

A scan has been performed with  $\beta \in [0, 2\%]$  and  $\hat{C} \in [0, 2.26]$  representing 680 SPEC calculations, each requiring approximately 24 CPU-hours on the MARCONI cluster<sup>1</sup>.

[Figure 3](#) shows some selected Poincaré sections at different values of  $\beta$  and  $\hat{C}$ , while [figure 4](#) shows the edge rotational transform, i.e. the rotational transform on the outer side of  $\Gamma_{PB}$ , as a function of  $\beta$  for four different values of  $\hat{C}$ .

For small values of  $\hat{C}$ , namely for  $\hat{C} < \hat{C}_{crit} \approx 0.59$ , the edge rotational transform decreases with increasing  $\beta$  and eventually reaches zero ([figure 4](#), black stars and red dots), at which point an  $m = 1$ ,  $n = 0$  island opens and forms a separatrix at the plasma boundary (see [figure 3a,c,e](#)). We will refer to this  $\beta$ -limit as the ideal equilibrium  $\beta$ -limit, denoted by  $\beta_{lim}^{ideal}$ , since it is well described by ideal MHD theory (see § 5.1). The value of  $\beta_{lim}^{ideal}$  obtained with SPEC is shown as a function of  $\hat{C}$  in [figure 5](#) (black triangles).

The ideal equilibrium  $\beta$ -limit can also be observed in tokamaks, although the underlying mechanism is different. In a tokamak, the plasma may be kept centred by applying a vertical magnetic field  $B_Z$ . As  $\beta$  grows,  $B_Z$  has to be increased, until it compensates the poloidal field  $B_p$  on the high field side. When this happens, the field is purely toroidal and a separatrix opens. In a stellarator, the poloidal magnetic field does not have to cancel everywhere for a separatrix to open, it merely has to be such that a field line never completes a poloidal turn. If this happens, the edge rotational transform is zero and a separatrix opens. In our calculations, the net toroidal current is constrained in the plasma volumes and at the interfaces. However, the actual dependencies of the current density on the toroidal and poloidal angle are unconstrained. Pfirsch–Schlüter and diamagnetic

<sup>1</sup><https://www.hpc.cineca.it/hardware/marconi>

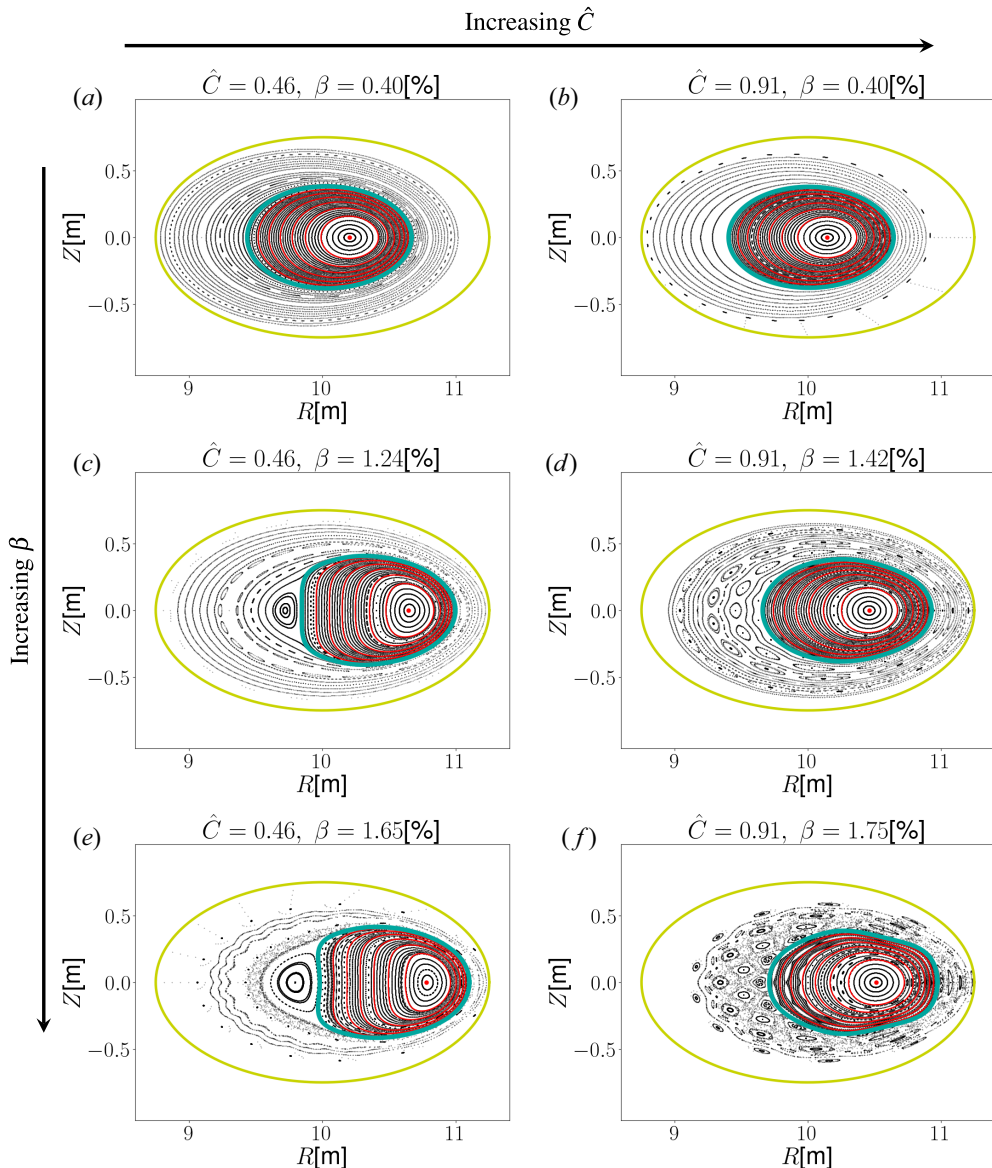


FIGURE 3. Poincaré plot (black dots) of equilibria at toroidal angle  $\phi = 0$  and at different values of  $(\beta, \hat{C})$ : (a,c,e)  $\hat{C} = 0.46$ ; (b,d,f)  $\hat{C} = 0.91$ . Red lines, inner plasma volume interfaces; blue line, plasma boundary; yellow line, computational boundary.

currents angular dependencies are the source of the poloidal magnetic field perturbation, the lowering of the edge rotational transform, and ultimately the opening of the separatrix. This is why, even in a zero net-toroidal-current stellarator ( $\hat{C} = 0$ ), the edge rotational transform reaches zero.

For values of  $\hat{C} > \hat{C}_{\text{crit}}$ , the (now strong enough) bootstrap current is able to prevent the edge rotational transform from reaching zero for any  $\beta$ , and hence no  $m = 1, n = 0$  island appears anywhere (see the blue crosses and green squares in figure 4). Instead, the

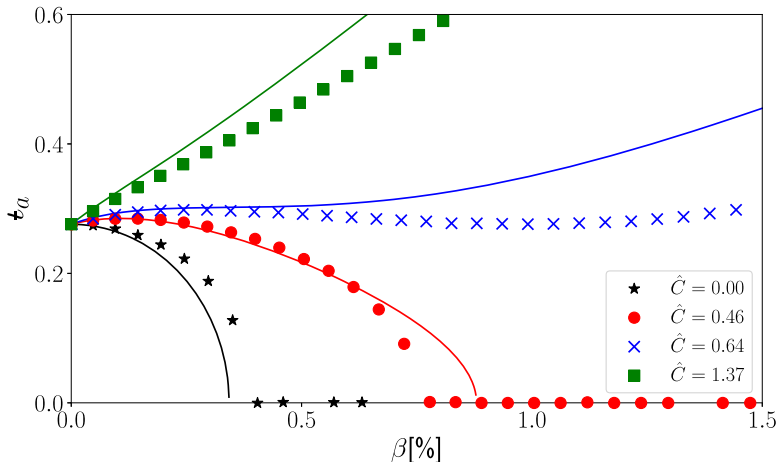


FIGURE 4. Edge rotational transform,  $t_a$ , as a function of plasma average  $\beta$ , for different values of  $\hat{C}$ ; stars, circles, crosses and squares are SPEC calculations while full lines are given by (5.1).

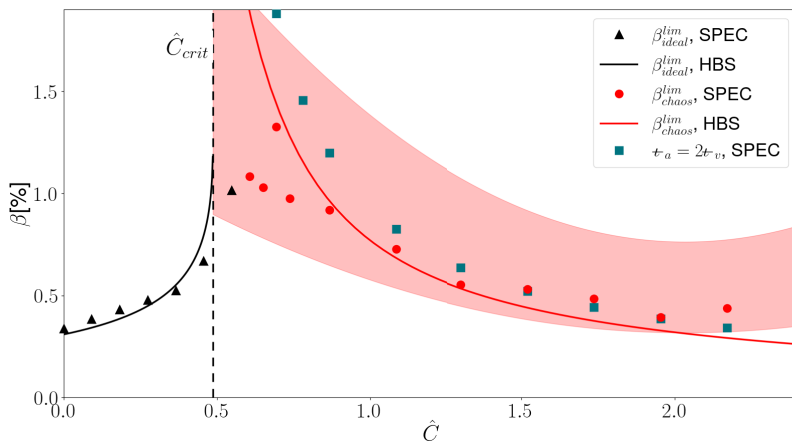


FIGURE 5. Equilibrium  $\beta$ -limit as a function of  $\hat{C}$ : black triangles, ideal equilibrium  $\beta$ -limit,  $\beta_{\text{lim}}^{\text{ideal}}$ , as obtained from SPEC; solid black line, analytical prediction for  $\beta_{\text{lim}}^{\text{ideal}}$  from (5.6); the dashed vertical line indicates the analytical value of  $\hat{C}_{\text{crit}}$  from (5.7); red dots, values of the chaotic equilibrium  $\beta$ -limit,  $\beta_{\text{lim}}^{\text{chaos}}$ , obtained from SPEC for  $B_{r,\text{crit}}/B = 10^{-5}$ ; the red area shows the range obtained from SPEC for  $B_{r,\text{crit}}/B \in [10^{-6}, 10^{-4}]$ ; solid red line, analytical prediction for  $\beta_{\text{lim}}^{\text{chaos}}$  obtained by solving (5.10); blue squares, SPEC values for which  $t_a = 2t_v$ .

edge rotational transform increases until many island chains open in the plasma and in the vacuum region (figure 3b,d,f). When these islands are large enough to have a significant impact on the radial transport, the chaotic equilibrium  $\beta$ -limit is reached, denoted by  $\beta_{\text{lim}}^{\text{chaos}}$ . Finally, for all values of  $\hat{C}$ , islands start to overlap and generate large regions of chaotic field lines at sufficiently large values of  $\beta$  (figure 3e,f). In § 4, a diagnostic to measure the critical value of  $\beta$  at which the chaotic equilibrium  $\beta$ -limit is reached will be presented, and an analytical model that explain the results will be derived in § 5.2.

It may be argued that volume interfaces might not be able to support the pressure if islands or chaos are close by (see, for example, figure 3f) – i.e. that SPEC equilibria might not be trusted at large  $\beta$  without further analyses. This question has been thoroughly studied in slab geometry by Qu *et al.* (2021). They identified two reasons why a solution might not exist.

The first possibility is that the magnetic surface does not exist, in particular that it is fractal. In our calculations above the equilibrium  $\beta$ -limit, large magnetic islands and chaotic regions develop close to volume interfaces. In this situation, it is indeed not known if the solution exists and additional analyses would be required, for example with convergence studies as proposed by Qu *et al.* (2021). Below the equilibrium  $\beta$ -limit, however, only small islands are present. The interfaces are not perturbed by neighbouring, large magnetic islands, and it is likely that the volume interfaces are magnetic surfaces. Since we are only interested in computing the equilibrium  $\beta$ -limit, it is sufficient to calculate equilibria below or equal to the equilibrium  $\beta$ -limit; larger  $\beta$  equilibria are irrelevant, and thus the question of existence of interfaces is eluded. In practice, we observe that large magnetic islands and chaotic field lines get close to the volume interfaces only for equilibria with  $\beta$  sufficiently large to trust the results presented in this paper. Nevertheless, convergence studies have been performed, and results presented in this paper have been shown to be spectrally converged (see the Appendix).

The second possibility is that the pressure jump on an interface is too large and a solution to the force-balance equation (2.2) does not exist. This is a possible explanation for when SPEC does not find an interface geometry that satisfies the force balance equation (2.2). However, in our calculations, SPEC finds magnetic geometries that do satisfy force balance. This means that the pressure jump across the interfaces is small enough and a solution exists. To summarize this discussion, we can trust the SPEC solutions presented in this paper.

#### 4. Measure of magnetic chaos and its effect on radial transport

##### 4.1. Fractal dimension, volume of chaos

One approach to discriminate between a chaotic field line and other magnetic field line topologies is to evaluate the fractal dimension  $D$  of the field line Poincaré section, for example using a box-counting algorithm (Meiss 1992). An almost binary behaviour is then observed: either a magnetic field line stays on a magnetic surface whose Poincaré section is a one-dimensional object,  $D = 1$ , or the magnetic field line has a fractal dimension  $D > D_{\text{crit}}$ , with  $1 < D_{\text{crit}} < 2$ . In our case, we observe that  $D_{\text{crit}} = 1.3$  can be used to differentiate between magnetic surfaces and chaos. Loizu *et al.* (2017) proposed to evaluate the volume occupied by chaotic field lines with

$$V_{\text{chaos}} = V_{\text{total}} \sum_{i=1}^{N_{\text{lines}}} \frac{(\psi_{t,i} - \psi_{t,i-1})}{\psi_a} \mathcal{H}(D_i - D_{\text{crit}}), \quad (4.1)$$

where  $N_{\text{lines}}$  is the number of considered field lines,  $D_i$  is the fractal dimension of the  $i$ th line,  $\mathcal{H}$  is the Heaviside function,  $V_{\text{total}}$  is the total plasma volume, and  $\psi_{t,i} - \psi_{t,i-1}$  measures the enclosed toroidal flux between field lines  $i$  and  $i - 1$ .

The chaotic equilibrium  $\beta$ -limit could then be defined as the  $\beta$  above which  $V_{\text{chaos}} > 0$ . The volume of chaos, however, while very useful as a measure of the number of chaotic field lines, does not provide enough information about whether or not the radial transport is enhanced by the destruction of magnetic surfaces. In addition, the volume of chaos is sensitive to the numerical resolution of the equilibrium – the larger the number of

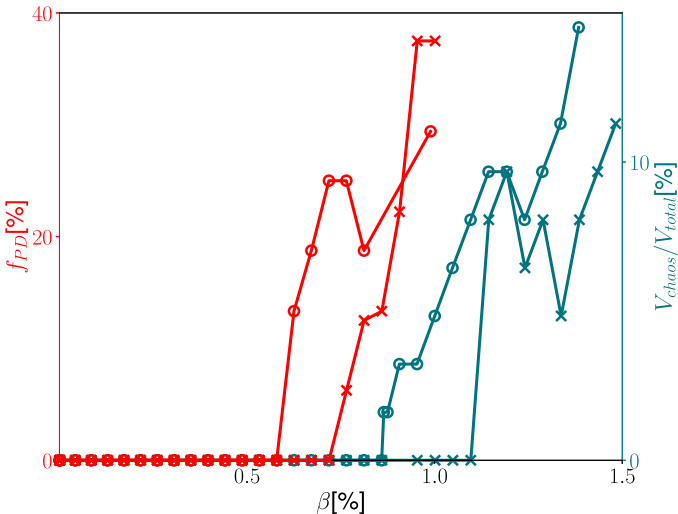


FIGURE 6. Here  $V_{chaos}/V_{total}$  (blue), and  $f_{PD}$  evaluated for  $B_{r,crit}/B = 10^{-5}$  (red) versus plasma averaged  $\beta$ , for  $M = N = 8$  (crosses) and  $M = N = 10$  (circles).

Fourier modes, the greater the number of potential resonances in the equilibrium. Due to overlap between small islands chains generated by high-order rationals, chaos may emerge at smaller  $\beta$  as the Fourier resolution is increased. For example, in figure 6 the volume of chaos is plotted as a function of  $\beta$  for two different Fourier resolutions,  $M = N = 8$  and  $M = N = 10$  (blue lines). We see that with this diagnostic, the measured chaotic equilibrium  $\beta$ -limit would drop from  $\sim 1.5\%$  to  $\sim 1\%$  if it were defined as the  $\beta$  above which  $V_{chaos} > 0$ . However, in the  $M = N = 10$  scan, some of the chaotic field lines are formed by high-order rationals and their associated smaller islands are expected to participate weakly with the radial transport, and could potentially be ignored. An alternative diagnostic that takes into account the effect of the magnetic field lines topology on the radial transport is thus required.

#### 4.2. Fraction of effective parallel diffusion

We discuss an alternative measure to the volume of chaos to determine if the destruction of magnetic surfaces significantly impacts the radial transport. Here the parallel and perpendicular direction are defined as the direction along and across the magnetic field, respectively, and the radial direction  $r$  as the direction perpendicular to isotherms,  $\nabla T \times \nabla r = 0$ , with  $T$  the temperature. In recent work, Paul *et al.* (2022) discussed the properties of the anisotropic heat diffusion equation,  $\nabla \cdot (\kappa_{\parallel} T + \kappa_{\perp} T) = 0$ , where  $\kappa_{\parallel}$  and  $\kappa_{\perp}$  are the parallel and perpendicular heat conductivities. In particular, Paul *et al.* demonstrated that, under the assumption that  $\kappa$  and  $\nabla \cdot \kappa$  are analytical, isotherms are topologically constrained to be toroidal surfaces – this forbids isotherms to align with the magnetic field in regions occupied by magnetic islands and magnetic field line chaos. Here  $\kappa$  is the diffusion tensor, defined as  $\kappa = \kappa_{\perp} I + (\kappa_{\parallel} - \kappa_{\perp}) BB/B^2$ , with  $I$  the identity tensor. Motivated by comparing the local parallel diffusion with the local perpendicular diffusion, Paul *et al.* introduced the volume of effective parallel diffusion, which is the volume of plasma where the parallel heat transport dominates perpendicular heat transport,

$$V_{PD} = \frac{1}{V_{total}} \int_{V_{total}} \mathcal{H}(\kappa_{\parallel} |\nabla_{\parallel} T|^2 - \kappa_{\perp} |\nabla_{\perp} T|^2) dx^3, \quad (4.2)$$

where the parallel and perpendicular gradients are defined as  $\nabla_{\parallel} = \mathbf{B}(\mathbf{B} \cdot \nabla)/B^2$  and  $\nabla_{\perp} = \nabla - \nabla_{\parallel}$ , respectively. In regions occupied by magnetic islands and magnetic field line chaos, the constraint on the isotherms topology implies that the magnetic field has a non-zero radial component, thus  $\nabla_{\parallel} T > 0$ . Depending on the ratio  $\kappa_{\parallel}/\kappa_{\perp}$ , the volume of effective parallel diffusion can then be greater than zero. On the contrary, in regions occupied by magnetic surfaces, isotherms largely coincide with magnetic surfaces, which means that  $\nabla_{\parallel} T$  is negligible, and consequently the volume  $V_{\text{PD}}$  is zero. Leveraging these properties, we can define the chaotic equilibrium  $\beta$ -limit as the  $\beta$  above which  $V_{\text{PD}} > 0$ .

To determine the chaotic equilibrium  $\beta$ -limit, it is only required to determine if  $V_{\text{PD}}$  is zero or not; its absolute value is irrelevant. We thus construct a proxy function for  $V_{\text{PD}}$  that does not depend on the temperature profile, but only on the magnetic field. We start by noticing that the Heaviside function in (4.2) is greater than zero when  $\kappa_{\parallel}|\nabla_{\parallel} T|^2 \geq \kappa_{\perp}|\nabla_{\perp} T|^2$ . As we expect the radial magnetic field to be small in comparison with the total magnetic field,  $B_r \ll B$ , we can write  $\nabla_{\parallel} T \sim \nabla T B_r/B$ , and  $\nabla_{\perp} T \sim \nabla T$ . The volume of effective parallel diffusion is then greater than zero if there is a finite volume where

$$\left(\frac{B_r}{B}\right)^2 \geq \frac{\kappa_{\perp}}{\kappa_{\parallel}} \equiv \left(\frac{B_{r,\text{crit}}}{B}\right)^2. \quad (4.3)$$

Considering the electron heat transport as a figure of merit for the confinement properties of the equilibrium, and using the Spitzer–Härm conductivity for  $\kappa_{\parallel,e}$  (Braginskii 1965), we get

$$\left(\frac{B_{r,\text{crit}}}{B}\right)^2 = 5.2 \times 10^{-22} \frac{n_e \log \Lambda \chi_{\perp,e}}{T_e^{5/2}}, \quad (4.4)$$

where  $\log \Lambda$  is the Coulomb logarithm, and typically  $\chi_{\perp,e} = \kappa_{\perp,e}/n_e \sim 1 \text{ m}^2 \text{ s}^{-1}$ . Here everything is to be expressed in SI units except  $T_e$ , which is in eV. For temperatures and densities between 1 to 10 keV and  $10^{19}$  to  $10^{20} \text{ m}^{-3}$ , respectively,  $B_{r,\text{crit}}/B$  ranges from  $10^{-6}$  to  $10^{-4}$ . For example using typical values for W7-X high performance experiments (Klinger *et al.* 2019), i.e.  $n_e = 4 \times 10^{19} \text{ m}^{-3}$ ,  $T_e = 5 \text{ keV}$ , we obtain a critical normalized radial magnetic field of  $B_{r,\text{crit}}/B \sim 10^{-5}$ . As a side note, we remark that the criterion (4.3) can also be derived by considering the radial heat diffusion equation for electrons,  $q_r = -\kappa_{\perp,e}(\nabla_{\perp} T_e)_r - \kappa_{\parallel,e}(\nabla_{\parallel} T_e)_r \sim -\kappa_{\perp,e} dT_e/dr - \kappa_{\parallel,e} dT_e/dr B_r^2/B^2$ . Magnetic islands and chaos play then an important role in setting the local heat radial transport when the second term on the right-hand side of the heat diffusion equation is larger than the first one, which occurs when  $B_r^2/B^2 \geq \kappa_{\perp}/\kappa_{\parallel}$ , recovering (4.3).

The volume of effective parallel diffusion can thus be written using the criterion (4.3),

$$V_{\text{PD}} \sim \frac{1}{V_{\text{total}}} \int_{V_{\text{total}}} \mathcal{H} \left( \left[ \frac{B_r}{B} \right]^2 - \left[ \frac{B_{r,\text{crit}}}{B} \right]^2 \right) dx^3. \quad (4.5)$$

This measure is, however, unpractical for the purpose of this paper, as it would require us to evaluate the radial magnetic field everywhere in the plasma. Instead, the radial magnetic field is evaluated where it is expected to be the largest, i.e. on a selected number of rational surfaces. We then construct the fraction of parallel diffusion,

$$f_{\text{PD}} = \frac{1}{N_{\text{res}}} \sum_{i=1}^{N_{\text{res}}} \mathcal{H} \left( \left[ \frac{B_r}{B} \right]^2 - \left[ \frac{B_{r,\text{crit}}}{B} \right]^2 \right), \quad (4.6)$$

where  $N_{\text{res}}$  is the number of considered resonances, and the algorithm used to evaluate the radial magnetic field  $B_r$  from SPEC equilibria is described in § 4.3. The fraction of

effective parallel diffusion is then the fraction of resonances in the plasma that contribute to the transport, i.e. the fraction of resonances over which the diffusion due to parallel dynamics dominates. Note that  $f_{\text{PD}} \neq V_{\text{PD}}$ , but if  $f_{\text{PD}} = 0$ , we can expect  $V_{\text{PD}}$  to be zero, and the opposite is true as well. The fraction of parallel diffusion can then be used as a proxy function to determine if the volume of parallel diffusion is zero or not. The chaotic equilibrium  $\beta$ -limit,  $\beta_{\lim}^{\text{chaos}}$ , is obtained by taking the value of  $\beta$  above which  $f_{\text{PD}} > 0$  (see figure 6).

Note that this does not define an equilibrium  $\beta$ -limit from an experimental point of view – the metric  $f_{\text{PD}}$  is positive as soon as one resonance satisfies (4.3), which would, in practice, only flatten the temperature and density profiles locally. It is certainly possible to increase the plasma averaged  $\beta$  further by increasing the input power. Our metric  $f_{\text{PD}}$ , however, informs us that the effect of field line topology starts to become important and has to be taken into account in transport calculations for  $\beta > \beta_{\lim}^{\text{chaos}}$ . One could imagine to combine the volume of chaos given by (4.1) with the criterion given by (4.3), and only consider resonances that span a sufficiently large volume and that contribute significantly to the radial transport. This idea will not be explored in this paper, and is left for future studies.

In practice, the metric  $f_{\text{PD}}$  is greater than zero when relatively small islands in comparison with the plasma minor radius emerge (using  $B_{r,\text{crit}}/B = 10^{-5}$ ). Thus, as long as the SPEC volumes are large enough to allow these islands to grow, the number of volumes does not affect the metric evaluation. In addition, given a sufficiently large number of volumes, the pressure profile is well resolved by the stepped-pressure approximation and thus the equilibrium does not depend strongly on the number of volumes (see the Appendix).

#### 4.3. Measure of the radial magnetic field

To evaluate the radial magnetic field  $B_r$ , it is useful to construct a general set of coordinates, such as quadratic flux minimizing (QFM) surfaces (Dewar, Hudson & Price 1994; Hudson & Dewar 1996, 1998), or ghost surfaces (Hudson & Dewar 2009), which have been shown to coincide with isotherms (Hudson & Breslau 2008). We construct QFM surfaces using the pyoculus package<sup>2</sup>. These surfaces, thereafter named  $\Gamma_{mn}$ , are smooth toroidal surfaces that pass through the X- and O-points of the island chain corresponding to the  $\iota = n/m$  rational resonant surface, and are constructed by finding the surfaces  $\Gamma_{mn}$  minimizing the weighted quadratic flux  $\int_{\Gamma_{mn}} w(\mathbf{B} \cdot \mathbf{n})^2 dS$ , where the weight  $w$  is cleverly chosen such that the underlying Euler–Lagrange equation has non-singular solutions. Some examples of QFM surfaces are plotted in figure 7. The radial coordinate  $r$  is then defined as the direction perpendicular to the QFM surfaces.

We can now measure the radial component of the magnetic field at each resonant surface  $\iota = n/m$ . We start by identifying all potential resonances  $(m, n) \in \mathbb{N}$  in each volume  $\mathcal{V}_l$  within the plasma boundary, such that (i)  $n/m$  is within the rotational transform extrema in the volume, and (ii)  $n$  is a multiple of the number of field periods. We construct QFM surfaces  $\Gamma_{mn}$  for each of the identified resonances  $\iota = n/m$ . The magnetic field perpendicular to the QFM surface,  $B_r$ , is obtained by projecting the magnetic field on their normal direction, and the magnetic field resonant harmonic,  $B_{r,mn}$  is obtained after a standard Fourier transform of  $B_r$ . Here, the poloidal angle is the straight-field line angle of the magnetic field tangential to the QFM surface. The Fourier spectrum of  $B_r$  is largely dominated by the  $(m, n)$  harmonic – it has been verified that  $B_{r,mn}$  is at least twice as large

<sup>2</sup><https://github.com/zhisong/pyoculus>

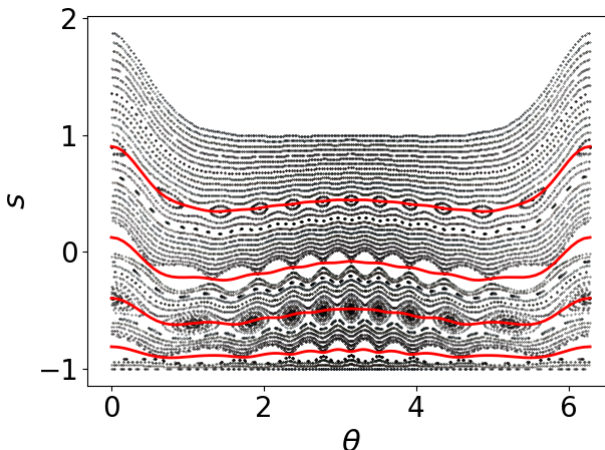


FIGURE 7. Black, Poincaré plot with magnetic surfaces and magnetic islands; red, QFM surface  $r = \text{const.}$  The coordinate  $s$  is a radial-like coordinate.

as the other Fourier harmonics of the radial magnetic field. We can thus assume  $B_r \approx B_{r,mn}$  to filter out numerical noise that may be generated by the QFM surface construction.

Only resonances with large radial magnetic field will significantly participate to the radial transport. Since the magnetic field harmonics  $B_{mn}$  are expected to decrease exponentially with the square of their mode numbers  $m$  and  $n$ , i.e.  $B_{mn} \sim \exp(-m^2 - n^2)$ , we can discard resonances with large poloidal and toroidal mode number and study only harmonics with mode number smaller than a given resolution,  $m \leq M_{\text{res}}$  and  $n \leq N_{\text{res}}$ . In this paper, we set  $M_{\text{res}} = 25$  and  $N_{\text{res}} = 10$ .

With the definition of the chaotic equilibrium  $\beta$ -limit from the fraction of effective parallel diffusion (4.6), only resonances with large radial magnetic field component matter; increasing the Fourier resolution of the equilibrium only introduces resonances with small radial magnetic field components, and thus has only a small impact on the value of  $f_{\text{PD}}$  – see for example the comparison between two  $\beta$ -scans with resolution  $M = N = 8$  and  $M = N = 10$  in figure 6 (red curves), and the chaotic equilibrium  $\beta$ -limit convergence study in the Appendix. Indeed, the critical  $\beta$  at which  $f_{\text{PD}}$  becomes larger than zero, namely  $\beta_{\lim}^{\text{chaos}}$ , becomes quite insensitive to the Fourier resolution for sufficiently large values of  $M$  and  $N$ , as the ones used for this paper ( $M = N = 12$ ). In that sense, this new diagnostic is more robust than the diagnostic based on the volume of chaos.

The chaotic equilibrium  $\beta$ -limit obtained using the metric  $f_{\text{PD}}$  defined in (4.6) is plotted in figure 5 with a red shaded area, spanning the range of  $\beta_{\lim}^{\text{chaos}}$  obtained when varying  $B_{r,\text{crit}}/B$  from  $10^{-6}$  to  $10^{-4}$ . The value of  $\beta_{\lim}^{\text{chaos}}$  obtained for  $B_{r,\text{crit}}/B = 10^{-5}$  is shown with red dots. We observe that the largest  $\beta$ -limit occurs at  $\hat{C} \approx 0.75$ . A small, but non-zero bootstrap current thus increases the equilibrium  $\beta$ -limit with respect to a classical stellarator without any net toroidal current ( $\hat{C} = 0$ ), and is thus beneficial.

## 5. Analytical prediction for the equilibrium $\beta$ -limits

We now derive an analytical model that predicts both the ideal and chaotic equilibrium  $\beta$ -limits. We make use of high- $\beta$  stellarator expansion theories derived by Wakatani (1998) and Freidberg (2014) to describe how the rotational transform at the plasma edge  $\tau_a$  evolves with  $\beta$ , taking into account the effect of the bootstrap current as well. Once a formula for

$\tau_a(\beta)$  has been derived, we can find whether an ideal  $\beta$ -limit is reached by solving  $\tau_a(\beta) = 0$ . When no solution is possible, a chaotic  $\beta$ -limit may also be estimated by assuming that the edge iota is modified by order one with respect to the vacuum rotational transform,  $\tau_a(\beta) - \tau_a(0) \sim \tau_a(0)$ , at which point it is likely that many resonances exist.

Assuming that (i)  $\epsilon \ll 1$ ,  $\delta = |B_p|/B_\phi \sim \epsilon^{3/4}$  with  $B_p$  the poloidal magnetic field,  $\beta \sim \epsilon$  and  $N_{fp} \sim \epsilon^{-1/2}$ , that (ii) magnetic surfaces are circular, and (iii) considering Solovev profiles for the pressure  $dP/d\psi_p = \text{const}$ , and the surface averaged toroidal current density  $\langle j_\phi \rangle = \text{const}$ , one can derive (Wakatani 1998; Freidberg 2014) an analytical model for the edge rotational transform,

$$\tau_a = (\tau_I + \tau_v)\sqrt{1 - \nu^2}, \quad (5.1)$$

$$\text{with } \tau_I = \frac{R_0}{2\psi_a} \mu_0 I_\phi(\beta) \quad (5.2)$$

$$\text{and } \nu = \frac{\beta}{\epsilon_a(\tau_I + \tau_v)^2}, \quad (5.3)$$

where  $I_\phi$  is the net toroidal current enclosed by the plasma and  $\tau_v$  is the edge rotational transform in a vacuum.

The bootstrap current model we employed in our equilibrium calculations (3.4) implies a linear relation between the net toroidal current in the system and the plasma  $\beta$ , thus

$$\tau_I = \sigma\beta, \quad (5.4)$$

where  $\sigma$  is a proportionality constant. It can be related to  $C$  by integrating (3.5) to compute  $I_\phi$  in (5.3), leading to

$$\sigma = \frac{2}{5} \frac{1}{\pi \epsilon_a^{3/2} \tau_v} \hat{C}. \quad (5.5)$$

Combining (5.1)–(5.5), analytical expressions of the edge rotational transform as a function of  $\beta$  for different values of  $\hat{C}$  can be obtained. Figure 4 compares the analytical curves with results obtained with SPEC. We observe reasonable agreement especially at low  $\beta$ . As  $\beta$  increases, however, (5.1) consistently underestimates the actual value of the rotational transform found by SPEC. Thus, even though the equilibrium constructed in § 3 does not exactly satisfy the assumptions used to derive (5.1), the assumptions are reasonable enough to use this analytical model to understand our numerical results. Equation (5.1) provides indeed an analytical (nonlinear) relation for  $\tau_a(\beta)$  which can be used to predict both the ideal and chaotic  $\beta$ -limits, as described in the following subsections.

### 5.1. Ideal equilibrium $\beta$ -limit

The solution to the relation  $\tau_a(\beta_{\lim}^{\text{ideal}}) = 0$  is given by

$$\beta_{\lim}^{\text{ideal}} = \frac{1}{\epsilon_a \sigma^2} \left[ \frac{1}{2} - \tau_v \epsilon_a \sigma - \sqrt{1 - 4\tau_v \epsilon_a \sigma} \right], \quad (5.6)$$

which is real for  $\sigma < (4\tau_v \epsilon_a)^{-1}$ , or

$$\hat{C} \leq \frac{5}{8} \frac{\psi_a}{\epsilon_a^{3/2} R_0^2 B_0} \equiv \hat{C}_{\text{crit}}. \quad (5.7)$$

Note the limit

$$\lim_{\sigma \rightarrow 0} \beta_{\lim}^{\text{ideal}} = \epsilon_a t_v^2, \quad (5.8)$$

retrieving the result from Freidberg (2014) and Loizu *et al.* (2017) for a zero-net-current stellarator ( $\hat{C} = 0$ ).

The curve  $\beta_{\lim}^{\text{ideal}}(\hat{C})$  is plotted in figure 5 with a black line. We observe that as  $\hat{C}$  increases, the ideal equilibrium  $\beta$ -limit increases. Comparison with data points measured from SPEC equilibria (red triangles) shows good agreement, especially for weaker bootstrap current ( $\hat{C} < 0.5$ ). The analytical value of  $\hat{C}_{\text{crit}} \approx 0.48$  is reasonably close to the one obtained with SPEC (smaller by approximately 18 %).

### 5.2. Chaotic equilibrium $\beta$ -limit

For larger values of  $\hat{C}$ , i.e.  $\hat{C} > \hat{C}_{\text{crit}}$ , the chaotic equilibrium  $\beta$ -limit is due to the emergence of chaos and its effectiveness in increasing the transport, thus estimating the chaotic equilibrium  $\beta$ -limit with (5.1) is not trivial – it is not known, *a priori*, which resonance will participate to the radial transport first. However, it is reasonable to assume that when the bootstrap current modifies the edge rotational transform by order one with respect to  $t_v$ , i.e.

$$\Delta t_a \equiv t_a - t_v = t_v, \quad (5.9)$$

magnetic islands and chaos are expected to appear. The values of  $\beta$  computed with SPEC at which the condition (5.9) is satisfied are plotted with brown squares in figure 5. We observe good agreement with the chaotic equilibrium  $\beta$ -limit (blue dots) for  $\hat{C} > 1$ .

We can also directly solve (5.9) using (5.1). We obtain a fourth-order polynomial equation for  $\beta$ ,

$$\beta^4 + 4\frac{t_v}{\sigma}\beta^3 + \left(2\frac{t_v^2}{\sigma^2} - \frac{1}{\epsilon_a^2\sigma^4}\right)\beta^2 - 4\frac{t_v^3}{\sigma^3}\beta - 3\left(\frac{t_v}{\sigma}\right)^4 = 0. \quad (5.10)$$

The real, positive root of (5.10) is plotted with a red line in figure 5. Direct comparison with the numerical data (blue squares) shows that (5.10) consistently underestimates the values of  $\beta$  that satisfy (5.9); this is a direct consequence of the underestimate of  $t_a$  by the analytical model (figure 4). The general dependence on  $\hat{C}$  is, however, recovered, capturing the chaotic equilibrium  $\beta$ -limit trend (red dots in figure 5) observed numerically for values of  $\hat{C} > 1$ . We remark that there are no free parameters in this analytical model. For  $\hat{C}_{\text{critical}} < \hat{C} < 1$ , the analytical model (5.10) overestimates greatly the chaotic equilibrium  $\beta$ -limit obtained with SPEC. In this transition region, the edge rotational transform depends weakly on  $\beta$  for  $\beta \lesssim 1$  (see, for example, the blue crosses in figure 4). As a consequence, the solution to (5.9) is large, and is therefore a bad estimate for the chaotic equilibrium  $\beta$ -limit. A more refined model would be required to better reproduce the results.

### 5.3. Dependence on design parameters

The edge rotational transform in a vacuum is approximately equal to the rotational transform on axis (low shear configuration), and can be estimated by a zeroth-order near

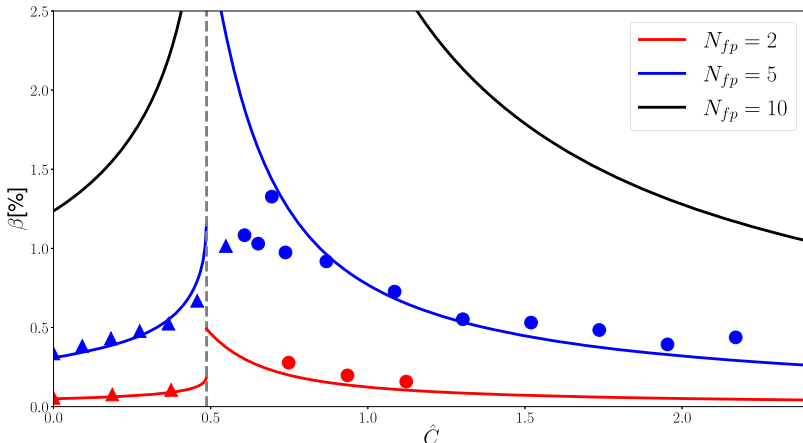


FIGURE 8. Analytical predictions of the equilibrium  $\beta$ -limit for different numbers of field period  $N_{fp}$ : full lines, ideal and chaotic equilibrium  $\beta$ -limits as predicted by (5.6) and (5.10), respectively; triangles and dots, ideal and chaotic equilibrium  $\beta$ -limits as obtained by SPEC, respectively.

axis expansion (Helander 2014; Loizu *et al.* 2017),

$$\tau_v^{\text{axis}} \approx \tau_v = \frac{N_{fp}}{2} \frac{(r_{\max} - r_{\min})^2}{r_{\max}^2 + r_{\min}^2}. \quad (5.11)$$

For low values of  $\hat{C}$ , the ideal equilibrium  $\beta$ -limit grows with the vacuum rotational transform (see (5.8)). For example, increasing the number of field periods increases  $\tau_v$ , thus also the equilibrium  $\beta$ -limit, as shown in figure 8. These results were corroborated by SPEC calculations with  $N_{fp} = 2$ , while calculations with  $N_{fp} = 10$  were difficult to achieve due to SPEC numerical fragility issues.

More generally, any mechanism that increases the rotational transform in a vacuum will increase the ideal and chaotic equilibrium  $\beta$ -limits. An increase in rotational transform can be achieved by either increasing the number of field periods, increasing the ellipse eccentricity (i.e. increasing the harmonic  $R_{11} = Z_{11}$ ) or adding some torsion to the magnetic axis. Magnetic axis torsion can, however, have a strong impact on the computed equilibrium, and additional studies would be required to see if it affects the conclusions of this paper.

Equation (5.7) gives  $\hat{C}_{\text{crit}} = 0.48$ , i.e. the equilibrium  $\beta$ -limit is maximized for a bootstrap current that has half the strength of the bootstrap current in an equivalent circular tokamak. Interestingly, if we approximate the total toroidal flux in the plasma as  $\psi_a \approx \pi a_{\text{eff}}^2 B_0$ , with  $B_0$  the modulus of the magnetic field on axis, we get  $\hat{C}_{\text{crit}} = 5\pi\sqrt{\epsilon_a}/8$ , which only depends on the inverse aspect ratio.

## 6. Conclusion

The SPEC code has been used to perform a large number of free-boundary stellarator equilibrium calculations including bootstrap current that allowed us to completely characterize classical stellarators in terms of their equilibrium  $\beta$ -limit. For configurations with low bootstrap current ( $\hat{C} < \hat{C}_{\text{crit}}$ ), an ideal equilibrium  $\beta$ -limit has been identified, where a central  $(m, n) = (1, 0)$  island appears. Stronger bootstrap current ( $\hat{C} > \hat{C}_{\text{crit}}$ ) prevents this central island from opening. Instead, a chaotic equilibrium  $\beta$ -limit is

reached, where the radial heat transport generated by pressure-induced magnetic islands and magnetic field line chaos competes with turbulence. We have implemented a proxy function to determine if the effective volume of parallel diffusion proposed by Paul *et al.* (2022) is greater than zero, thereby assessing the impact of the field line topology on radial transport and deducing the equilibrium  $\beta$ -limit from SPEC equilibrium calculations.

An analytical model showed good agreement with the ideal equilibrium  $\beta$ -limit obtained numerically for weak bootstrap current. The general trend for the chaotic equilibrium  $\beta$ -limit could also be extracted for stronger bootstrap current, up to  $\hat{C} \sim 2$ . Analytical insights provided ways to predict the effect of design parameters on the equilibrium  $\beta$ -limit; for example, the ideal  $\beta$ -limit has been shown to increase with  $\hat{C}$ , while the chaotic equilibrium  $\beta$ -limit decreases with  $\hat{C}$ , thereby showing a peak equilibrium  $\beta$ -limit around  $\hat{C}_{\text{crit}}$ . The critical value of  $\hat{C}_{\text{crit}}$  depends only on the inverse aspect ratio, under reasonable assumptions.

To improve the equilibrium  $\beta$ -limit of stellarators, optimization of different parameters can be performed. For example, Landreman, Medasani & Zhu (2021*b*) recently coupled SPEC with the simsopt framework (Landreman *et al.* 2021*a*) to perform optimization for good magnetic surfaces at the same time as quasisymmetry in a vacuum, and Baillod *et al.* (2022) showed that good magnetic surfaces can be recovered in finite  $\beta$ , finite current equilibria by modifying either the plasma boundary, the coils, or by injecting a toroidal current in the plasma. Applying the same recipe to a sequence of equilibria with increasing  $\beta$ , one can optimize a stellarator configuration for larger equilibrium  $\beta$ -limit. Note, however, that the fraction  $f_{\text{PD}}$  is generally not a smooth function of the equilibrium and might not be a good target function for optimization. Another smooth function should be developed from the radial magnetic field component  $B_r$  if one desires to minimize the impact of field line topology on radial transport.

Future studies will focus on more exotic stellarator geometries, for example configurations optimized for quasisymmetry or quasi-isodynamicity, and include self-consistent bootstrap currents, as proposed by Landreman, Buller & Drevlak (2022). Finally, one could use the SPEC code to evaluate the stability limit for different values of  $\hat{C}$ , using the methods developed by Kumar *et al.* (2021, 2022). This would provide useful information on the dependence of the stability limit on the parameter  $\hat{C}$ , and allow comparison with the equilibrium  $\beta$ -limit.

## Acknowledgements

The authors thank P. Helander, S.R. Hudson, C. Zhu, J. Schilling, J. Cazabonne and E. Balkovic for useful discussions. This work was supported in part by the Swiss National Science Foundation.

*Editor P. Helander thanks the referees for their advice in evaluating this article.*

## Funding

This work has been carried out within the framework of the EUROfusion Consortium, via the Euratom Research and Training Programme (grant agreement no. 101052200 – EUROfusion) and funded by the Swiss State Secretariat for Education, Research and Innovation (SERI). Views and opinions expressed are, however, those of the author(s) only and do not necessarily reflect those of the European Union, the European Commission or SERI. Neither the European Union nor the European Commission nor SERI can be held responsible for them. This research was supported by a grant from the Simons Foundation (1013657, J.L.).

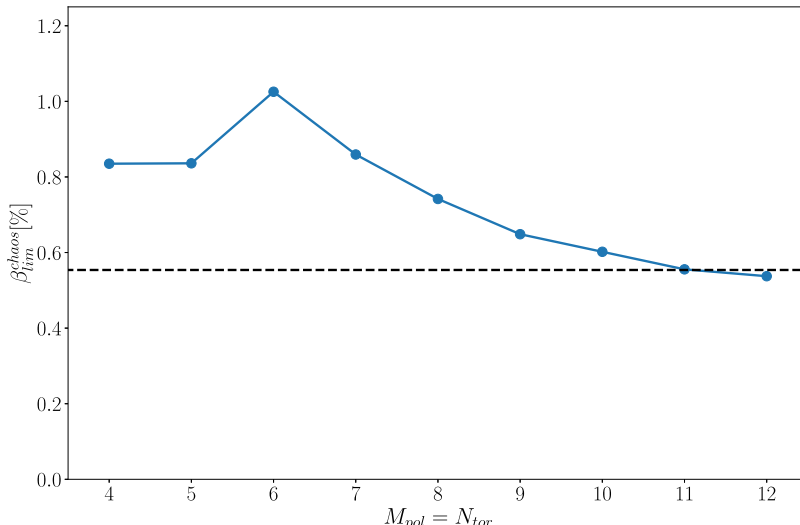


FIGURE 9. Chaotic equilibrium  $\beta$ -limit, as obtained by SPEC for  $B_{r,crit}/B_0 = 10^{-6}$ , and  $\hat{C} = 1.37$  as a function of the equilibrium Fourier resolution. The black, dashed line is the analytical prediction obtained by solving (5.10).

#### Data availability statement

The data that support the findings of this study are available from the corresponding author upon reasonable request.

#### Declaration of interests

The authors report no conflict of interest.

#### Appendix. Convergence on numerical resolution and number of volumes

The chaotic equilibrium  $\beta$ -limit, as obtained by SPEC for  $B_{r,crit}/B_0 = 10^{-6}$ , and  $\hat{C} = 1.37$ , is plotted on figure 9 as a function of the equilibrium Fourier resolution. Convergence towards a value close to the analytical prediction is observed. The resolution used to compute the results presented in this paper, i.e.  $M_{pol} = N_{tor} = 12$ , seems large enough so that the relative variations obtained by further increasing the Fourier resolution become small, of the order of 3 %.

We now discuss the dependence of the ideal and the chaotic equilibrium  $\beta$ -limit dependence on the number of volumes  $N_{vol}$ . Keeping the same coil shapes and currents, we approximate the pressure profile  $p = p_0(1 - \psi_t/\psi_a)$  with different numbers of interfaces supporting an equal pressure step,  $[[p]]_l = p_0/N_{vol}$ . We set  $I_{\phi,l}^v = 0$  and  $I_{\phi,l}^s$  following the bootstrap current model described in (3.4). A large range of  $\beta$  is scanned for  $\hat{C} = 0.46 < \hat{C}_{crit}$  and  $\hat{C} = 1.37 > \hat{C}_{crit}$ , and for  $N_{vol} = \{2, 4, 6, 8, 10, 12\}$ . The corresponding ideal and chaotic equilibrium  $\beta$ -limits obtained from SPEC are shown on figure 10.

For  $\hat{C} = 0.45$ , an ideal equilibrium  $\beta$ -limit is found, that grows with the number of volumes, asymptotically approaching the analytical prediction as obtained by (5.6). This is expected, as ideal MHD is recovered as the number of volumes approaches infinity (Dennis *et al.* 2013a). Interestingly, we observe variations of the chaotic equilibrium  $\beta$ -limit of the order of 30 % as the number of volumes is changed, clearly within the range of values covered when  $B_{r,crit}$  is varied. The dependence of the chaotic equilibrium  $\beta$ -limit is thus

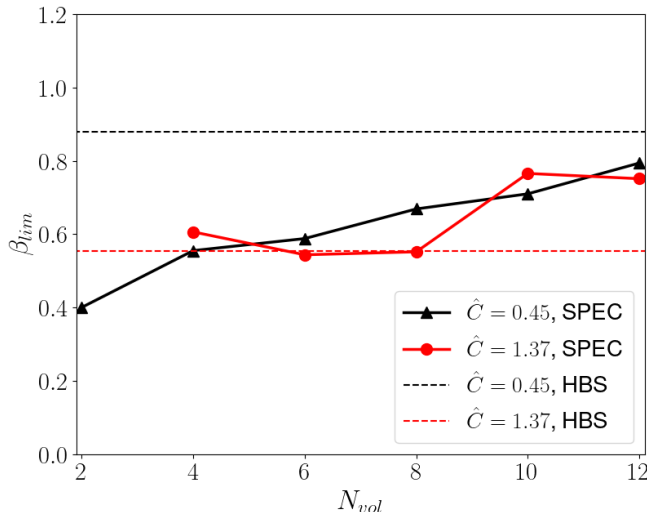


FIGURE 10. Dependence of the equilibrium  $\beta$ -limit on the number of volumes  $N_{vol}$ : black, ideal equilibrium  $\beta$ -limit, obtained for  $\hat{C} = 0.45$ ; red, chaotic equilibrium  $\beta$ -limit, obtained for  $\hat{C} = 1.37$ ; full lines, equilibrium  $\beta$ -limit, as obtained with SPEC; dashed line, analytical prediction, as obtained with the HBS theory.

negligible in comparison with its dependence on  $B_{r,crit}$ , i.e. on the plasma temperature and densities. We conclude that the stepped-pressure assumption made by the SPEC model has few to no consequences on the physical results presented in this paper.

## REFERENCES

- BAILLOD, A., LOIZU, J., GRAVES, J.P. & LANDREMAN, M. 2022 Stellarator optimization for nested magnetic surfaces at finite  $\beta$  and toroidal current. *Phys. Plasmas* **29** (4), 042505.
- BAILLOD, A., LOIZU, J., QU, Z.S., KUMAR, A. & GRAVES, J.P. 2021 Computation of multi-region, relaxed magnetohydrodynamic equilibria with prescribed toroidal current profile. *J. Plasma Phys.* **87** (4), 905870403.
- BHATTACHARJEE, A., HAYASHI, T., HEGNA, C.C., NAKAJIMA, N. & SATO, T. 1995 Theory of pressure-induced islands and self-healing in three-dimensional toroidal magnetohydrodynamic equilibria. *Phys. Plasmas* **2** (3), 883–888.
- BRAGINSKII, S.I. 1965 Transport Processes in a Plasma. *Rev. Plasma Phys.* **1**, 205.
- CARY, J.R. & HANSON, J.D. 1986 Stochasticity reduction. *Phys. Fluids* **29** (8), 2464.
- CARY, J.R. & KOTSCHENREUTHER, M. 1985 Pressure induced islands in three-dimensional toroidal plasma. *Phys. Fluids* **28** (5), 1392–1401.
- DENNIS, G.R., HUDSON, S.R., DEWAR, R.L. & HOLE, M.J. 2013a The infinite interface limit of multiple-region relaxed magnetohydrodynamics. *Phys. Plasmas* **20** (3), 032509.
- DENNIS, G.R., HUDSON, S.R., DEWAR, R.L. & HOLE, M.J. 2014 Multi-region relaxed magnetohydrodynamics with anisotropy and flow. *Phys. Plasmas* **21** (7), 072512.
- DENNIS, G.R., HUDSON, S.R., TERRANOVA, D., FRANZ, P., DEWAR, R.L. & HOLE, M.J. 2013b Minimally constrained model of self-organized helical states in reversed-field pinches. *Phys. Rev. Lett.* **111** (5), 055003.
- DEWAR, R.L., HUDSON, S.R. & PRICE, P.F. 1994 Almost invariant manifolds for divergence-free fields. *Phys. Lett. A* **194** (1), 49–56.
- FREIDBERG, J.P. 2014 *Ideal MHD*. Cambridge University Press.
- GRIEGER, G., RENNER, H. & WOBIG, H. 1985 Wendelstein stellarators. *Nucl. Fusion* **25** (9), 1231–1242.

- HELANDER, P. 2014 Theory of plasma confinement in non-axisymmetric magnetic fields. *Rep. Prog. Phys.* **77** (8), 087001.
- HELANDER, P. & SIGMAR, D.J. 2002 *Collisional Transport in Magnetized Plasmas*. Cambridge University Press.
- HUANG, Y.-M., HUDSON, S.R., LOIZU, J., ZHOU, Y. & BHATTACHARJEE, A. 2022 Numerical study of  $\delta$ -function current sheets arising from resonant magnetic perturbations. *Phys. Plasmas* **29** (3), 032513.
- HUDSON, S.R. & BRESLAU, J. 2008 Temperature contours and ghost surfaces for chaotic magnetic fields. *Phys. Rev. Lett.* **100** (9), 1–4.
- HUDSON, S.R. & DEWAR, R.L. 1996 Almost-invariant surfaces for magnetic field-line flows. *J. Plasma Phys.* **56** (2), 361–382.
- HUDSON, S.R. & DEWAR, R.L. 1998 Construction of an integrable field close to any non-integrable toroidal magnetic field. *Phys. Lett. A* **247** (3), 246–251.
- HUDSON, S.R. & DEWAR, R.L. 2009 Are ghost surfaces quadratic-flux-minimizing? *Phys. Lett. A* **373** (48), 4409–4415.
- HUDSON, S.R., DEWAR, R.L., HOLE, M.J. & MCGANN, M. 2012 Non-axisymmetric, multi-region relaxed magnetohydrodynamic equilibrium solutions. *Plasma Phys. Control. Fusion* **54**, 014005.
- HUDSON, S.R., LOIZU, J., ZHU, C., QU, Z.S., NÜHRENBERG, C., LAZERSON, S., SMIET, C.B. & HOLE, M.J. 2020 Free-boundary MRxMHD equilibrium calculations using the stepped-pressure equilibrium code. *Plasma Phys. Control. Fusion* **62** (8), 084002.
- HUDSON, S.R. & NAKAJIMA, N. 2010 Pressure, chaotic magnetic fields, and magnetohydrodynamic equilibria. *Phys. Plasmas* **17** (5), 052511.
- KLINGER, T., ANDREEVA, T., BOZHENKOV, S., BRANDT, C., BURHENN, R., BUTTENSCHÖN, B., FUCHERT, G., GEIGER, B., GRULKE, O., LAQUA, H.P., et al. 2019 Overview of first Wendelstein 7-X high-performance operation. *Nucl. Fusion* **59** (11), 112004.
- KUMAR, A., NÜHRENBERG, C., QU, Z., HOLE, M.J., DOAK, J., DEWAR, R.L., HUDSON, S.R., LOIZU, J., ALEYNIKOVA, K., BAIILOD, A., et al. 2022 Nature of ideal MHD instabilities as described by multi-region relaxed MHD. *Plasma Phys. Control. Fusion* **64** (6).
- KUMAR, A., QU, Z., HOLE, M.J., WRIGHT, A.M., LOIZU, J., HUDSON, S.R., BAIILOD, A., DEWAR, R.L. & FERRARO, N.M. 2021 Computation of linear MHD instabilities with the multi-region relaxed MHD energy principle. *Plasma Phys. Control. Fusion* **63** (4).
- LANDREMAN, M., BULLER, S. & DREVLAK, M. 2022 Optimization of quasi-symmetric stellarators with self-consistent bootstrap current and energetic particle confinement. *Phys. Plasmas* **29** (8), 082501.
- LANDREMAN, M., MEDASANI, B., WECHSUNG, F., GIULIANI, A., JORGE, R. & ZHU, C. 2021a SIMSOPT: a flexible framework for stellarator optimization. *J. Open Source Softw.* **6** (65), 3525.
- LANDREMAN, M., MEDASANI, B. & ZHU, C. 2021b Stellarator optimization for good magnetic surfaces at the same time as quasisymmetry. *Phys. Plasmas* **28** (9), 092505.
- LANDREMAN, M., SMITH, H.M., MOLLÉN, A. & HELANDER, P. 2014 Comparison of particle trajectories and collision operators for collisional transport in nonaxisymmetric plasmas. *Phys. Plasmas* **21** (4), 042503.
- LOIZU, J., HUANG, Y.-M., HUDSON, S.R., BAIILOD, A., KUMAR, A. & QU, Z.S. 2020 Direct prediction of nonlinear tearing mode saturation using a variational principle. *Phys. Plasmas* **27** (7), 070701.
- LOIZU, J., HUDSON, S., BHATTACHARJEE, A. & HELANDER, P. 2015a Magnetic islands and singular currents at rational surfaces in three-dimensional magnetohydrodynamic equilibria. *Phys. Plasmas* **22** (2), 022501.
- LOIZU, J. & HUDSON, S.R. 2019 Multi-region relaxed magnetohydrodynamic stability of a current sheet. *Phys. Plasmas* **26** (3), 030702.
- LOIZU, J., HUDSON, S.R., BHATTACHARJEE, A., LAZERSON, S. & HELANDER, P. 2015b Existence of three-dimensional ideal-magnetohydrodynamic equilibria with current sheets. *Phys. Plasmas* **22** (9), 090704.
- LOIZU, J., HUDSON, S.R., HELANDER, P., LAZERSON, S.A. & BHATTACHARJEE, A. 2016a Pressure-driven amplification and penetration of resonant magnetic perturbations. *Phys. Plasmas* **23** (5), 055703.

- LOIZU, J., HUDSON, S.R. & NÜHRENBERG, C. 2016*b* Verification of the SPEC code in stellarator geometries. *Phys. Plasmas* **23** (11), 112505.
- LOIZU, J., HUDSON, S.R., NÜHRENBERG, C., GEIGER, J. & HELANDER, P. 2017 Equilibrium  $\beta$ -limits in classical stellarators. *J. Plasma Phys.* **83** (6), 715830601.
- MEISS, J.D. 1992 Symplectic maps, variational principles, and transport. *Rev. Mod. Phys.* **64** (3), 795–848.
- PAUL, E.J., HUDSON, S.R. & HELANDER, P. 2022 Heat conduction in an irregular magnetic field. Part 2. Heat transport as a measure of the effective non-integrable volume. *J. Plasma Phys.* **88** (1), 905880107.
- PEDERSEN, T.S., OTTE, M., LAZERSON, S., HELANDER, P., BOZHENKOV, S., BIEDERMANN, C., KLINGER, T., WOLF, R.C. & BOSCH, H.-S. 2016 Confirmation of the topology of the Wendelstein 7-X magnetic field to better than 1:100,000. *Nat. Commun.* **7** (1), 13493.
- QU, Z.S., DEWAR, R.L., EBRAHIMI, F., ANDERSON, J.K., HUDSON, S.R. & HOLE, M.J. 2020*a* Stepped pressure equilibrium with relaxed flow and applications in reversed-field pinch plasmas. *Plasma Phys. Control. Fusion* **62** (5), 054002.
- QU, Z.S., HUDSON, S.R., DEWAR, R.L., LOIZU, J. & HOLE, M.J. 2021 On the non-existence of stepped-pressure equilibria far from symmetry. *Plasma Phys. Control. Fusion* **63** (12).
- QU, Z.S., PFEFFERLÉ, D., HUDSON, S.R., BAILLOD, A., KUMAR, A., DEWAR, R.L. & HOLE, M.J. 2020*b* Coordinate parametrization and spectral method optimisation for Beltrami field solver in stellarator geometry. *Plasma Phys. Control. Fusion* **62** (12), 124004.
- RECHESTER, A.B. & ROSENBLUTH, M.N. 1978 Electron heat transport in a tokamak with destroyed magnetic surfaces. *Phys. Rev. Lett.* **40** (1), 38–41.
- REIMAN, A., ZARNSTORFF, M.C., MONTICELLO, D., WELLER, A., GEIGER, J. & THE W7-AS TEAM 2007 Pressure-induced breaking of equilibrium flux surfaces in the W7AS stellarator. *Nucl. Fusion* **47** (7), 572–578.
- SUZUKI, Y., WATANABE, K.Y. & SAKAKIBARA, S. 2020 Theoretical studies of equilibrium beta limit in LHD plasmas. *Phys. Plasmas* **27** (10), 102502.
- TAYLOR, J.B. 1974 Relaxation of toroidal plasma and generation of reverse magnetic fields. *Phys. Rev. Lett.* **33** (19), 1139–1141.
- TAYLOR, J.B. 1986 Relaxation and magnetic reconnection in plasmas. *Rev. Mod. Phys.* **58** (3), 741–763.
- WAKATANI, M. 1998 *Stellarator and Heliotron Devices*, International Series of Monographs on Physics, vol. 95. Oxford University Press.